An anisotropic viscoelastic-viscoplastic model for short-fiber composites

An Anisotropic Viscoelastic-Viscoplastic Model for Short-Fiber Composites

A. Amiri-Rad[1,2], L.V. Pastukhov[1,2], L.E. Govaert[1], and J.A.W. van Dommelen[1]

[1]Eindhoven University of Technology, P.O. Box 513, 5600 MB, Eindhoven, the Netherlands

[2]Dutch Polymer Institute (DPI), P.O. Box 902, 5600 AX, Eindhoven, the Netherlands

1 Abstract

In this paper, an anisotropic viscoelastic-viscoplastic macro-mechanical model is presented for short-fiber reinforced polymers. In addition to the rate-dependent response of the polymer matrix, fiber orientation leads to elastic and plastic anisotropy in short-fiber composites. The dependence of the yield stress on the strain rate and on the orientation is modeled by use of the Hill equivalent stress and the Eyring flow rule. Uniaxial tests at various strain rates were performed on injection molded samples cut at different orientations with respect to the mold flow direction. The test results show that the effects of strain rate and material orientation on yield stress are factorizable.

The model aims to capture this behavior, which simplifies the characterization process. First, the model with a single relaxation time is presented and then the model is extended to multiple relaxation times to improve the predictions in the pre-yield regime. An efficient method for finding the model parameters for different modes is presented. An implicit scheme is used for the integration of the constitutive equations and the derivation of the consistent tangent stiffness tensor is presented. The model is implemented as an ABAQUS user material (UMAT) subroutine and is validated through comparison of the simulation results with the experiments.

2 Introduction

Faster and more cost-effective production of components based on short-fiber reinforced polymers (SFRP) has led to an increase in their popularity compared to other structural composites. They can be used to produce complex geometries with relatively high specific strength and stiffness and are appealing to a variety of industries. Their light weight is particularly interesting to the automotive industry to increase efficiency and reduce CO_2 emission. Some examples of automotive parts produced by SFRP are air intake manifolds, cooling parts, front-ends, and engine mounts.

A particularity of short-fiber filled systems is the anisotropy of the elastic and plastic properties that is caused by flow-induced fiber orientation during injection molding [1–3]. Additionally, the time-dependent behavior of the polymer matrix adds to the complexity of the mechanical response. Reliable prediction of the mechanical behavior of the final product is a requirement

in the design process.

The underlying microstructure has a major effect on the mechanical properties of SFRPs. Linking the effective material properties to the underlying microstructure can be done by closed-form or computational homogenization techniques. Mean-field methods are closed-form techniques which have been vastly utilized in the study of multi-phase materials. Some examples from this category are [4–8]. This group of models usually assume a simplified structure with certain restrictions on the material behavior, fiber alignment, fiber geometry and size, number of material phases, etc. For example, simplified morphologies such as fibers with the same size and orientation or a single inclusion in an infinite matrix are assumed. Computational homogenization techniques have also been widely used in the study of reinforced materials [9–11]. They enable the application of more complex and realistic RVEs, but are computationally much more demanding.

Other than multi-scale models, continuum-based macro-scale models may be also a favorable choice for the prediction of the mechanical response of the SFRPs. They require less computational resources and can provide accurate predictions. Amongst the numerous works on the macro-scale constitutive modeling of polymer composites, the rate-dependent plastic response is usually ignored [12, 13]. In this paper, an anisotropic macro-scale model for the material yield kinetics will be presented.

The model proposed in this study is based on a generic framework for describing the time-dependent mechanical response of polymers. Pioneered by the work of Haward and Thackray [14], a group of models was developed for polymers which do not use an explicit yield surface and instead the tran-

sition to the plastic regime is imposed by an exponential dependence of the relaxation time on stress. Further developments to this model followed, where major contributions were made by the groups of Boyce (BPA model) [15–17], Buckley (OGR model) [18–20] and our group in Eindhoven [21–23], referred to as the Eindhoven Glassy Polymer (EGP) model.

In the present study, an extension of the EGP model is presented which captures the dependence of the yield stress on the material orientation and the strain rate. While the dependence of the yield stress on both of these variables may seem to complicate the characterization process, the model is constructed in a way such that the material parameters can be determined in a simple process. Using uniaxial experiments in different material orientations and strain rates, it is demonstrated that the effects of orientation and strain rate on the yield stress are factorizable and therefore they can be taken apart. In the presented model, these effects are effectively decoupled which leads to a simpler characterization process.

Van Erp *et al.* [24] presented an associated flow rule which uses Hill's anisotropic effective stress along with the Eyring model for viscoplasticity. They successfully applied this model to oriented polypropylene to predict the yield behavior. Senden *et al.* [25] incorporated the formulation presented by van Erp *et al.* [24] to the EGP framework which was previously used for modeling isotropic glassy polymers. In this paper, this model will be extended to predict the anisotropic and rate-dependent elastic and yield behavior of short-fiber reinforced polymers. The objective of this paper is to develop a model for the anisotropic viscoelastic-viscoplastic behavior of SFRPs. An efficient method is presented for obtaining the model parameters. Further-

more, the numerical implementation in the finite element framework and the derivation of the consistent stiffness matrix are presented. In addition to short-fiber composites, the proposed model could also be used for other anisotropic and time-dependent systems, which show the same factorizable behavior, such as semi-crystalline polymers.

This paper is organized in the following order. First, the experimental observations and the constitutive model are presented. Next, the implicit scheme used for the numerical implementation and the model characterization are discussed. In the next part, the predictive abilities of the model are validated using the experimental results at different strain rates and orientations. Finally, the model is extended to a multi-mode version for a more accurate representation of the pre-yield response.

3 Experimental

In this section, the results of the performed uniaxial tests for different strain rates and material orientations are presented. First, the material and test method are explained and then the observations are discussed.

3.1 Material and Sample Preparation

The material used in this study is a 20 wt.% short E-glass fiber reinforced polycarbonate (SABIC Lexan® 3412R PC) provided by SABIC Innovative Plastics, Bergen op Zoom, the Netherlands. Injection=molded plaques were prepared for material characterization (265 mm length, 70 mm width, 3 mm thickness). The gating system and plaque geometry facilitate shear flow

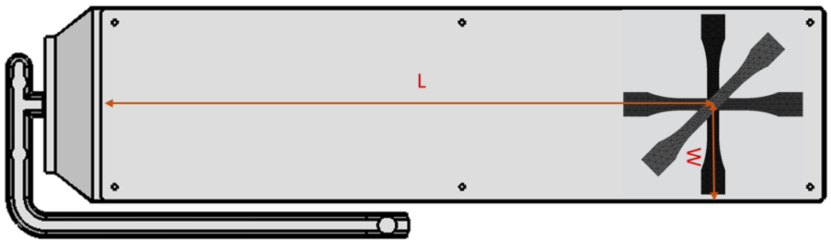

Figure 1: Geometry of the injection molded plaques and the uniaxial samples cut at different orientations.

resulting in higher fiber orientation and degree of anisotropy. Specimens were cut from injection molded plaques at different angles with respect to the flow direction at one location and machined (milled) to a dog-bone shape according to ISO 527 Type 1BA. The specimens were cut from the end of the plaques, where processing simulations showed less variation in the fiber orientation throughout the specimens. The position at which specimens were taken is shown in Figure 1, where L = 180 mm (distance from the gate) and W = 35 mm (distance from the edge).

3.2 Mechanical Tests

Uniaxial tensile tests were performed using Zwick Z010 Material Testing Machines, equipped with a 5 kN load cell and a Zwick videoXtens non-contact extensometer. All experiments were done at room temperature (23 °C, 40%RH). To characterize the deformation kinetics, uniaxial tensile tests were performed at strain rates ranging from 10^{-6} s^{-1} up to 10^{-2} s^{-1}. Engineering stresses were calculated using the average of the cross-sectional surface area as measured at three locations in the gauge section. The engineering strain was calculated from measurements of the distance between

markers attached to the sample surface with the video extensometer. In order to determine the Poisson's ratio, samples were painted with a speckle pattern, and strain measurements were done using a Zeiss Discovery V20 optical microscope and analyzed by a global 2D-DIC (digital image correlation) technique. The creep tests were performed at constant load and, therefore, the constant engineering stress. To avoid overshoot effects, the load was slowly applied in 10 seconds.

3.3 Results

The results of the uniaxial tests show a dependence of the yield stress on orientation and strain rate. Figure 2 (a) shows experimental data (markers) along with fitted curves for yield stress vs. strain rate in a log-log plot. The angle ϕ represents the angle between the longitudinal direction of the sample and the first principal material direction which aligns with the mold flow direction. As it is observed in this figure, when the yield stress vs. strain rate data are plotted on a log-log scale, by change of material orientation, the slope of the curves remains the same and the curves are only shifted along the vertical axis. This shows that the effects of the orientation and the strain rate on the yield stress are factorizable. The factorizable dependence of the yield stress σ_y on strain rate $\dot{\varepsilon}$ and material orientation ϕ in a uniaxial test can be expressed as follows:

$$\sigma_y = f(\dot{\varepsilon})g(\phi). \tag{1}$$

The developed constitutive model presented in the next section aims to

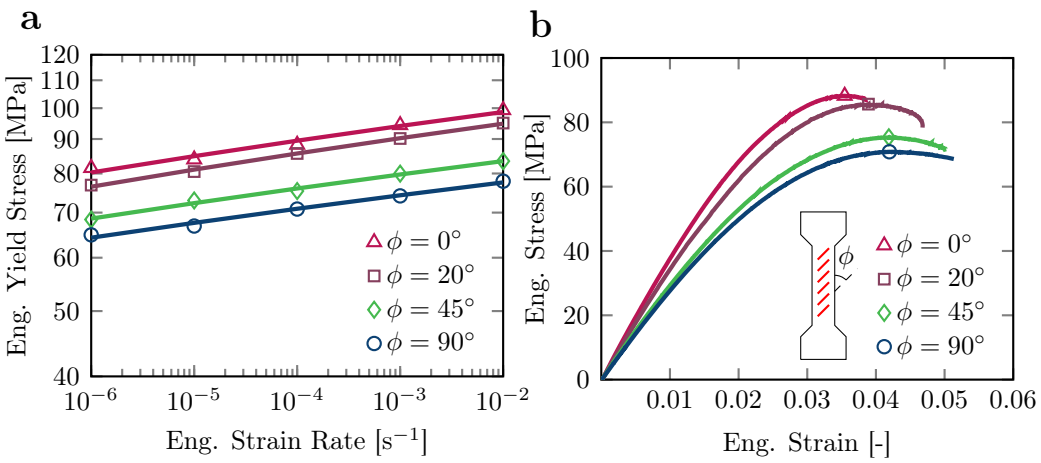

Figure 2: (a) Yield stress at different strain rates and material orientations for polycarbonate with 20 wt.% glass fiber; solid lines are guides to the eye (b) uniaxial test results for different material orientations at a constant strain rate of 10^{-4} s^{-1} for polycarbonate with 20 wt.% glass fiber.

capture this effect. First, the model is presented with a single relaxation time, which needs considerably shorter simulation times. The extension of the model to multiple relaxation times, which in addition to yield stress also captures the nonlinear pre-yield response with a very good accuracy, is also presented. The results for uniaxial tests for different material orientations at the constant strain rate of 10^{-4} s^{-1} are shown in Figure 2 (b). As shown in this figure, the elastic response is also anisotropic and additionally it is nonlinear. While the single-mode model presents a more simplified approach in which the elastic regime is described linearly, the multi-mode model aims to capture the nonlinearity in the elastic regime.

4 Single-Mode Model

In this section, first the set of constitutive equations for the single-mode model is presented and then the numerical implementation is discussed. The extension of the model to multiple relaxation times is presented in the next section.

4.1 Constitutive Model

The model presented here is in line with the EGP framework, which is based on the pioneering work of Haward and Thackray [14] who proposed two parallel contributions. The first one, called the driving stress, is the result of the intermolecular interactions of secondary bonds and is the major contributing factor in the viscoelastic behavior. The second one, called the hardening stress, originates from the elastic response of the entangled network of primary bonds and becomes significant in the post-yield regime. Instead of using an explicit yield surface, the viscosity is exponentially reduced by increasing stress, employing an Eyring equation [26]. Plastic flow at yield is regarded as a stress-induced glass transition.

The mechanical analog of the constitutive model is shown in Figure 3. As shown in this figure, the model consists of a Maxwell branch and a parallel neo-Hookean spring. In the current model, both the spring and the dashpot in the Maxwell branch are anisotropic. Although the model includes a branch responsible for hardening, the ability of the model to predict the hardening in the post-yield regime is not validated in this paper and focus is placed on the prediction of the initial yield behavior.

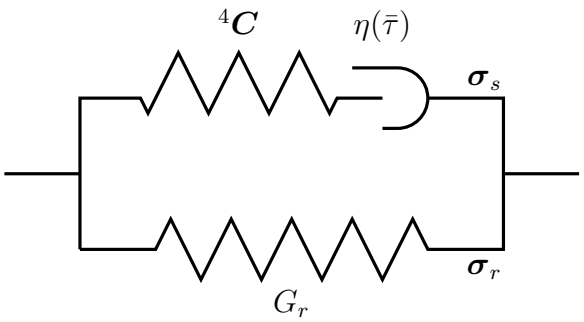

Figure 3: Mechanical analog of the anisotropic constitutive model.

For the Maxwell branch, a multiplicative decomposition of the deformation gradient tensor $\boldsymbol{F}$ into the elastic and plastic components is used. It is assumed that first, a plastic deformation $\boldsymbol{F}_p$ transforms the initial configuration $\mathcal{C}_i$ to an intermediate stress-free state $\hat{\mathcal{C}}$ and then an elastic deformation $\boldsymbol{F}_e$ is applied which brings the material to its current configuration $\mathcal{C}_c$. To make sure that the decomposition is unique, it is assumed that the plastic part of the deformation contains no rigid body rotation i.e. $\boldsymbol{R}_p = \boldsymbol{I}$ [15]:

$$\boldsymbol{F} = \boldsymbol{F}_e \cdot \boldsymbol{F}_p. \tag{2}$$

Following this decomposition, the velocity gradient tensor $\boldsymbol{L}$ can be written as:

$$\boldsymbol{L} = \dot{\boldsymbol{F}} \cdot \boldsymbol{F}^{-1} = \dot{\boldsymbol{F}}_e \cdot \boldsymbol{F}_e^{-1} + \boldsymbol{F}_e \cdot \dot{\boldsymbol{F}}_p \cdot \boldsymbol{F}_p^{-1} \cdot \boldsymbol{F}_e^{-1}. \tag{3}$$

Using this equation, the elastic and plastic velocity gradient tensors in the current configuration can be defined:

$$\boldsymbol{L}_e = \dot{\boldsymbol{F}}_e \cdot \boldsymbol{F}_e^{-1}, \tag{4}$$

$$\boldsymbol{L}_p = \boldsymbol{F}_e \cdot \dot{\boldsymbol{F}}_p \cdot \boldsymbol{F}_p^{-1} \cdot \boldsymbol{F}_e^{-1}. \tag{5}$$

The symmetric part of $\dot{\boldsymbol{F}}_p \cdot \boldsymbol{F}_p^{-1}$ is defined as the plastic rate of deformation tensor in the intermediate configuration:

$$\hat{\boldsymbol{D}}_p = \mathrm{sym}(\dot{\boldsymbol{F}}_p \cdot \boldsymbol{F}_p^{-1}). \tag{6}$$

As described before (Figure 3), the total stress $\boldsymbol{\sigma}$ is split into two components, driving stress $\boldsymbol{\sigma}_s$ and hardening stress $\boldsymbol{\sigma}_r$ [14]:

$$\boldsymbol{\sigma} = \boldsymbol{\sigma}_s + \boldsymbol{\sigma}_r. \tag{7}$$

The hardening stress $\boldsymbol{\sigma}_r$ is calculated according to:

$$\boldsymbol{\sigma}_r = \frac{G_r}{J} \tilde{\boldsymbol{B}}^d, \tag{8}$$

where G_r is the neo-Hookean hardening modulus, J is the volume ratio and $\tilde{\boldsymbol{B}}^d$ is the deviatoric part of the isochoric left Cauchy-Green deformation tensor:

$$\begin{aligned} \tilde{\boldsymbol{B}} &= J^{-2/3} \boldsymbol{B}, \\ \tilde{\boldsymbol{B}}^d &= \tilde{\boldsymbol{B}} - \frac{1}{3} \mathrm{tr}(\tilde{\boldsymbol{B}}) \boldsymbol{I}. \end{aligned} \tag{9}$$

The driving stress component $\boldsymbol{\sigma}_s$, is the stress in the Maxwell branch

(Figure 3). In the EGP model, the elastic response of the material is assumed to be isotropic and the spring in the Maxwell branch is ruled by an isotropic neo-Hookean law. This neo-Hookean spring is replaced by an anisotropic linear elastic one. For calculating the stress tensor from the linear anisotropic law, first the driving stress tensor $\boldsymbol{\sigma}_s$ is pulled back to the intermediate configuration and is expressed as the second Piola-Kirchhoff stress tensor $\hat{\boldsymbol{S}}_s$:

$$\hat{\boldsymbol{S}}_s = J\boldsymbol{F}_e^{-1} \cdot \boldsymbol{\sigma}_s \cdot \boldsymbol{F}_e^{-T}. \tag{10}$$

This stress tensor is related to the elastic Green-Lagrange strain tensor:

$$\hat{\boldsymbol{E}}_e = \frac{1}{2}(\boldsymbol{F}_e^T \cdot \boldsymbol{F}_e - \boldsymbol{I}), \tag{11}$$

by the following equation:

$$\hat{\boldsymbol{S}}_s = {}^4\hat{\boldsymbol{C}} : \hat{\boldsymbol{E}}_e. \tag{12}$$

The components of the anisotropic elastic stiffness tensor ${}^4\hat{\boldsymbol{C}}$ are defined in the intermediate configuration. Assuming orthotropic elasticity, the 4th order elastic stiffness tensor in the material coordinate system can be written as a matrix using the Voigt notation [27]:

$$\underline{\check{C}} = \begin{pmatrix} \frac{1-\nu_{23}\nu_{32}}{E_{22}E_{33}\Delta} & \frac{\nu_{21}+\nu_{31}\nu_{23}}{E_{22}E_{33}\Delta} & \frac{\nu_{31}+\nu_{21}\nu_{32}}{E_{22}E_{33}\Delta} & 0 & 0 & 0 \\ \frac{\nu_{12}+\nu_{13}\nu_{32}}{E_{11}E_{33}\Delta} & \frac{1-\nu_{31}\nu_{13}}{E_{11}E_{33}\Delta} & \frac{\nu_{32}+\nu_{31}\nu_{12}}{E_{11}E_{33}\Delta} & 0 & 0 & 0 \\ \frac{\nu_{13}+\nu_{12}\nu_{23}}{E_{11}E_{22}\Delta} & \frac{\nu_{23}+\nu_{13}\nu_{21}}{E_{11}E_{22}\Delta} & \frac{1-\nu_{12}\nu_{21}}{E_{11}E_{22}\Delta} & 0 & 0 & 0 \\ 0 & 0 & 0 & G_{12} & 0 & 0 \\ 0 & 0 & 0 & 0 & G_{23} & 0 \\ 0 & 0 & 0 & 0 & 0 & G_{13} \end{pmatrix}, \tag{13}$$

where

$$\Delta = \frac{1 - \nu_{12}\nu_{21} - \nu_{23}\nu_{32} - \nu_{31}\nu_{13} - 2\nu_{12}\nu_{23}\nu_{31}}{E_{11}E_{22}E_{33}}. \tag{14}$$

This stiffness matrix includes 9 independent material constants. The Cauchy stress $\boldsymbol{\sigma}_s$ in the Maxwell branch can be found from the 2nd Piola-Kirchhoff stress from the inverse of Equation (10).

Knowing the stress in the Maxwell branch, the rate of plastic deformation can be found using a flow rule. In the original EGP model, the plastic flow direction is found using a generalized non-Newtonian flow relation. To extend the model to include anisotropic plasticity, following van Erp *et al.* [24], an associated flow rule is used where the direction of the plastic flow is obtained from the derivative of the equivalent stress $\bar{\tau}$ with respect to the stress tensor in the intermediate configuration:

$$\hat{\boldsymbol{D}}_p = \dot{\bar{\gamma}}_p \hat{\boldsymbol{N}}, \tag{15}$$

$$\hat{\boldsymbol{N}} = \frac{\partial \bar{\tau}}{\partial \hat{\boldsymbol{S}}_s}, \tag{16}$$

where $\hat{\boldsymbol{D}}_p$ is the plastic rate of deformation tensor in the intermediate configuration (Equation (6)). The equivalent rate of the plastic flow $\dot{\bar{\gamma}}_p$ is found from the Eyring equation [28]:

$$\dot{\bar{\gamma}}_p = \frac{\bar{\tau}}{\eta}, \tag{17}$$

where η is the viscosity and can be calculated from the following equation:

$$\eta = \eta_0 a(\bar{\tau}), \tag{18}$$

where η_0 is the zero shear viscosity and the variable $a(\bar{\tau})$ is called the stress shift factor:

$$\eta_0 = \frac{\tau_0}{\dot{\gamma}_0}, \tag{19}$$

$$a(\bar{\tau}) = \frac{\bar{\tau}/\tau_0}{\sinh(\bar{\tau}/\tau_0)}. \tag{20}$$

This equation only takes into account the effect of stress on viscosity. The effects of temperature, pressure and aging ([21]) are not considered here. In this equation, $\bar{\tau}$ is the equivalent stress, $\dot{\gamma}_0$ is the rate constant and τ_0 is called the characteristic stress.

In the isotropic EGP model [21–23], the equivalent stress $\bar{\tau}$ is found from the von Mises effective stress $\bar{\sigma}$:

$$\bar{\tau} = \frac{\bar{\sigma}}{\sqrt{3}}. \tag{21}$$

Following Van Erp *et al.* [24], in the anisotropic model, the equivalent stress $\bar{\tau}$ is found from the effective stress of Hill analogous to Equation (21). The effective stress in the Hill's plasticity model is expressed as [29]:

$$\begin{aligned}\bar{\sigma}_H^2 =& F(\check{S}_{s,22} - \check{S}_{s,33})^2 + G(\check{S}_{s,33} - \check{S}_{s,11})^2 + H(\check{S}_{s,11} - \check{S}_{s,22})^2 \\ &+ 2L\check{S}_{s,23}^2 + 2M\check{S}_{s,13}^2 + 2N\check{S}_{s,12}^2,\end{aligned} \tag{22}$$

where

$$\begin{aligned} F &= \frac{1}{2}\left(\frac{1}{R_{22}^2} + \frac{1}{R_{33}^2} - \frac{1}{R_{11}^2}\right);\ L = \frac{3}{2R_{23}^2}; \\ G &= \frac{1}{2}\left(\frac{1}{R_{11}^2} + \frac{1}{R_{33}^2} - \frac{1}{R_{22}^2}\right);\ M = \frac{3}{2R_{13}^2}; \\ H &= \frac{1}{2}\left(\frac{1}{R_{11}^2} + \frac{1}{R_{22}^2} - \frac{1}{R_{33}^2}\right);\ N = \frac{3}{2R_{12}^2}, \end{aligned} \tag{23}$$

where $\check{S}_{s,ij}$ are stress components obtained by transformation of the stress tensor $\hat{S}_{s,ij}$ to the material coordinate system. The constants R_{11}, R_{22} and R_{33} are ratios of the yield stress in different principal material directions to the reference yield stress $\sigma_{y,ref}$. Values R_{12}, R_{23} and R_{13} are ratios of shear yield stresses to the reference shear yield stress $\tau_{y,ref} = \frac{\sigma_{y,ref}}{\sqrt{3}}$.

4.2 Numerical Implementation

An implicit scheme is used for the integration of the set of constitutive equations presented in the previous section. In this section, this implicit scheme for the calculation of the stress tensor $\boldsymbol{\sigma}$ at the end of a time step for a given deformation gradient $\boldsymbol{F}$ will be presented.

The integration scheme is started with an initial estimate for the plastic right Cauchy-Green deformation tensor $\boldsymbol{C}_{p_{n+1}}$. Then, the value of the plastic

right stretch tensor $\boldsymbol{U}_{p_{n+1}}$ at the end of the time step t_{n+1} is calculated according to:

$$\boldsymbol{U}_{p_{n+1}} = \sqrt{\boldsymbol{C}_{p_{n+1}}}. \tag{24}$$

With the plastic right stretch tensor $\boldsymbol{U}_{p_{n+1}}$ known, the elastic deformation gradient tensor $\boldsymbol{F}_{e_{n+1}}$ and the driving stress tensor can be calculated from:

$$\boldsymbol{F}_{e_{n+1}} = \boldsymbol{F}_{n+1} \cdot \boldsymbol{U}_{p_{n+1}}^{-1}, \tag{25}$$

and Equations (11) and (12). For finding the stress shift factor a, the equivalent stress $\bar{\tau}_{n+1}$ is found explicitly from its value at t_n. This is beneficial when extending the model to the multi-mode version (section 5). The explicit calculation of the equivalent stress makes it possible to calculate the stress tensor in each mode independent of the other modes for each step. This makes the integration process simpler and more cost-effective:

$$\bar{\tau}_{n+1} = \bar{\tau}_n + \dot{\bar{\tau}}_n \Delta t, \tag{26}$$

$$\dot{\bar{\tau}}_n = \frac{\partial \bar{\tau}}{\partial \boldsymbol{F}} : \dot{\boldsymbol{F}}_n, \tag{27}$$

where the derivative of the equivalent stress $\bar{\tau}$ with respect to the deformation gradient $\boldsymbol{F}$ can be found from the derivation presented in the Appendix. The stress shift factor is then calculated from Equation (20). Using Equations (15) to (19), the plastic rate of deformation $\hat{\boldsymbol{D}}_{p_{n+1}}$ can be found. Next, the rate of the plastic right Cauchy-Green deformation tensor $\dot{\boldsymbol{C}}_{p_{n+1}}$ is ob-

tained according to:

$$\dot{\boldsymbol{C}}_{p_{n+1}} = 2\boldsymbol{U}_{p_{n+1}} \cdot \hat{\boldsymbol{D}}_{p_{n+1}} \cdot \boldsymbol{U}_{p_{n+1}}. \tag{28}$$

The value of the plastic right Cauchy-Green deformation tensor at the time t_{n+1} is then obtained from the following Euler backward integration:

$$\boldsymbol{C}_{p_{n+1}} = \boldsymbol{C}_{p_n} + \Delta t \dot{\boldsymbol{C}}_{p_{n+1}}. \tag{29}$$

This set of equations is solved with the Newton-Raphson scheme. In each step, an initial guess will be made for the value of $\boldsymbol{C}_{p_{n+1}}$ and the residual is calculated by finding the difference between this value and the value found from Equation (29). The model is implemented as a user material subroutine (UMAT) in the finite element package ABAQUS. The derivation of the consistent tangent stiffness matrix is presented in the Appendix.

4.3 Characterization

As was mentioned in the previous sections, the effects of strain rate and orientation on yield stress are factorizable and the model is constructed to take advantage of this observation to make the characterization simpler. As a result, finding the dependence on the strain rate for a single orientation and the dependence on orientation for a single strain rate are enough to fully characterize the yield behavior of the material.

For finding the Eyring constants (kinetics parameters) which determine the dependence of the yield stress on the strain rate, the Eyring equation (Equation (17)) can be applied to the uniaxial test results at different strain

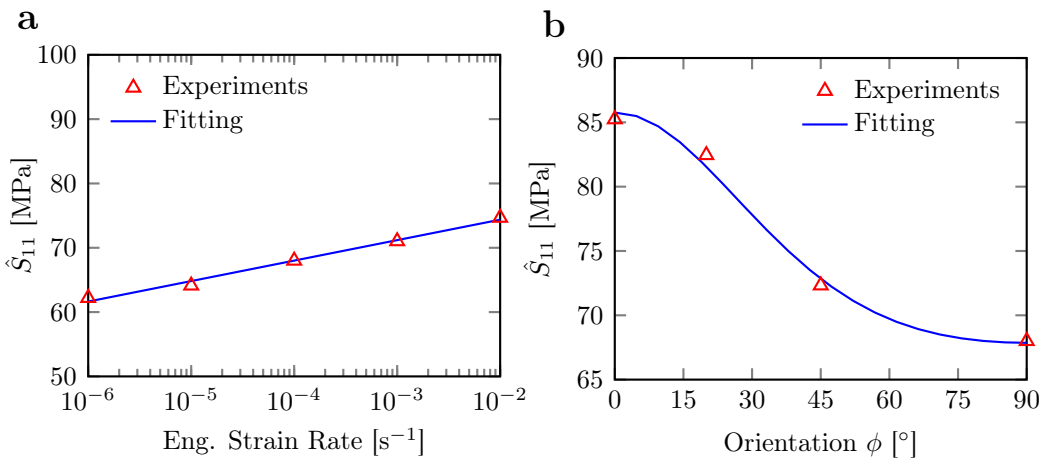

Figure 4: (a) Yield stress at different strain rates for the orientation $\phi = 90°$; (b) yield stress for different orientations at the strain rate of 10^{-4} s^{-1} : experimental data and the fitted curve.

rates. The Eyring equation can be rewritten in the following form and it is obvious that on a semi-logarithmic scale it represents a straight line where slope and height can be fitted to the experimental data:

$$\bar{\sigma} = \sigma_0 \ln(10) \log(\dot{\bar{\varepsilon}}_p) + \sigma_0 \ln\left(\frac{2}{\dot{\varepsilon}_0}\right), \tag{30}$$

where $\sigma_0 = \sqrt{3}\tau_0$ and $\dot{\varepsilon}_0 = \frac{\dot{\gamma}_0}{\sqrt{3}}$. Fitting of the Eyring equation to the experimental data for the polycarbonate with 20 wt.% glass fiber (section 3) is shown in Figure 4 (a). Yield stress versus strain rate at $\phi = 90°$ is used. The values obtained for the characteristic stress τ_0 and the rate constant $\dot{\gamma}_0$ are shown in Table 1.

The next set of parameters required for the characterization of the yield response are the plastic anisotropy parameters (constants in the Hill's equation, see Equations (22) to (23)). Here, the reference yield stress is chosen

Table 1: Model parameters.

Kinetics		Plastic Anisotropy			Elastic Anisotropy			
$\dot{\gamma}_0$ [s^{-1}]	τ_0 [MPa]	R_{11}	R_{22}	R_{12}	E_{11} [MPa]	E_{22} [MPa]	G_{12} [MPa]	$\nu_{12} = \nu_{23}$
1.48×10^{-25}	0.8	1.26	1	1.1	2348	1589	650	0.26

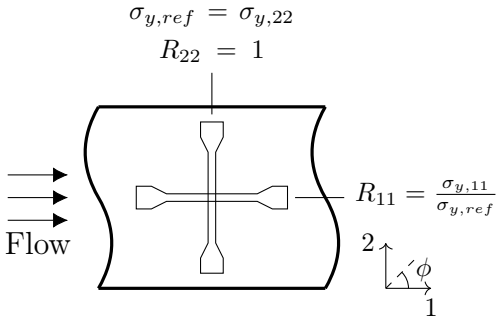

Figure 5: Calculation of the Hill constants from yield stress values in different orientations.

as the yield stress in the 2 direction $\sigma_{y,ref} = \sigma_{y,22}$ (Figure 5). In the samples used for testing, fibers are mostly oriented in 1 direction (mold flow direction) and therefore, the yield stress decreases from a maximum in the 1 direction to a minimum in the 2 direction.

For finding these parameters, Hill's equation can be applied to the yield stress vs. material orientation data at a constant strain rate. Here, the assumption of transverse isotropy is used. For a transversely isotropic material, only the R_{11} and R_{12} parameters need to be found. It is worth mentioning that, by choosing direction 2 as the reference direction, $R_{22} = 1$ and that the yield stress in the 2 direction for any strain rate is already known using the obtained kinetics parameters. For a plane stress uniaxial test, the following equation can be derived between the yield stress and the material direction:

$$\sigma_y = \sigma_{y,ref}(\dot{\bar{\varepsilon}})g(\phi),$$
$$g(\phi) = \left[F\sin^4\phi + G\cos^4\phi + H(\cos^2\phi - \sin^2\phi)^2 + 2N\sin^2\phi\cos^2\phi\right]^{-\frac{1}{2}}, \tag{31}$$

where σ_{y} is the uniaxial yield stress at angle ϕ and $\sigma_{y,ref}$ is the reference yield stress. As it is seen in this equation, the Hill formulation enables a multiplicative decomposition of the effects of strain rate and orientation. Figure 4 (b) shows the Hill equation fitted to the experimental data at the strain rate of 10^{-4} s^{-1}. The obtained Hill parameters are shown in Table 1.

With the assumption of transverse isotropy, 5 elastic constants E_{11}, E_{22}, G_{12}, ν_{12} and ν_{23} are also required. Considering the kinetics parameters and plastic anisotropy parameters determined previously, in total 10 material parameters are required for a transversely isotropic material. Since uniaxial experiments are used here and only in-plane loading exists, ν_{23} is not determined and its value in simulations is taken equal to ν_{12}. Although here, the assumption of transverse isotropy is used, the model is a general orthotropic model and can be applied to a fully orthotropic material system.

4.4 Results and Discussion

As was described in the previous section, the yield stress vs. strain rate at $\phi = 90^\circ$ and the yield stress vs. orientation at a strain rate of 10^{-4} s^{-1} are used for material characterization. As a validation, yield stress for other strain rates and orientations are predicted using the implemented model and a comparison is made with the experimental data. A 2D plane stress uniax-

ial dog-bone sample is constructed in ABAQUS and a constant strain rate loading is applied. Figure 6 shows the model predictions and the experimental data. Yield stress for different strain rates and material orientations are plotted on a log-log scale. It should be noted that some plastic deformation happens prior to the maximum load and the yield stress is not defined as the point where plasticity occurs for the first time, but it is defined as the maximum stress.

Factorizable dependence of the yield stress on strain rate and material orientation means that the dependence of the yield stress on the material orientation does not change with the strain rate and vice versa. Therefore, after finding Hill's constants for a single strain rate and kinetic parameters for a single orientation, the model should be able to predict the yield stress for an arbitrary orientation and strain rate. As shown in Figure 6, model predictions for other strain rates and orientations are in good agreement with the experiments.

Creep tests are performed on the samples with $\phi = 0^\circ$ and $\phi = 90^\circ$ material orientations (Figure 7). It is observed that the log-log plot of the applied stress vs. time-to-failure has the same but negative slope as the log-log plot of yield stress vs. strain rate (Figure 2). This implies that, as observed in polymers without reinforcement [30–32], time-to-failure multiplied by the secondary creep strain rate is a constant. Additionally, this indicates that the state of deformation during secondary creep is the same as that at yield in a constant rate experiment. This is also previously observed for polymers without reinforcement [33,34]. Creep simulations are performed in ABAQUS

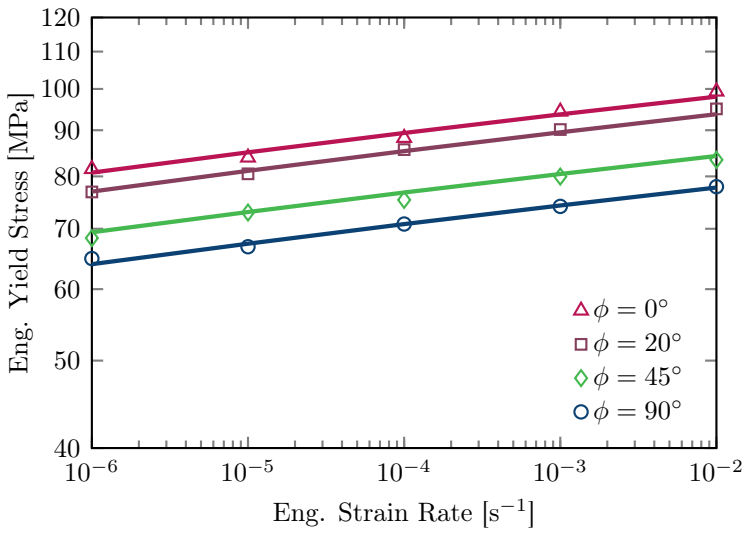

Figure 6: Model predictions (solid-lines) vs. experimental data (markers) for yield stress at different strain rates and material orientations.

using the developed model and the results are compared with the experiments in Figure 7 (a). The evolution of strain in the simulations at different stress levels for $\phi = 0°$ is shown in Figure 7 (b). In the simulations, failure is considered as a point where the strain rate increases significantly and the strain localization happens. The failure points are shown by markers in Figure 7 (b). As it is observed, a good agreement exists between simulation and experimental results. The stress dependence of the time-to-failure for any direction can be predicted using the characterization performed using constant rate experiments (Figure 4). This is very useful since constant rate experiments are easier to perform and no other characterization is required.

Figure 8 shows stress-strain curves for different angles at a constant strain rate of 10^{-4} s^{-1}. As it is observed from these curves, no strain hardening is considered in the simulations, since the uniaxial tension tests show local-

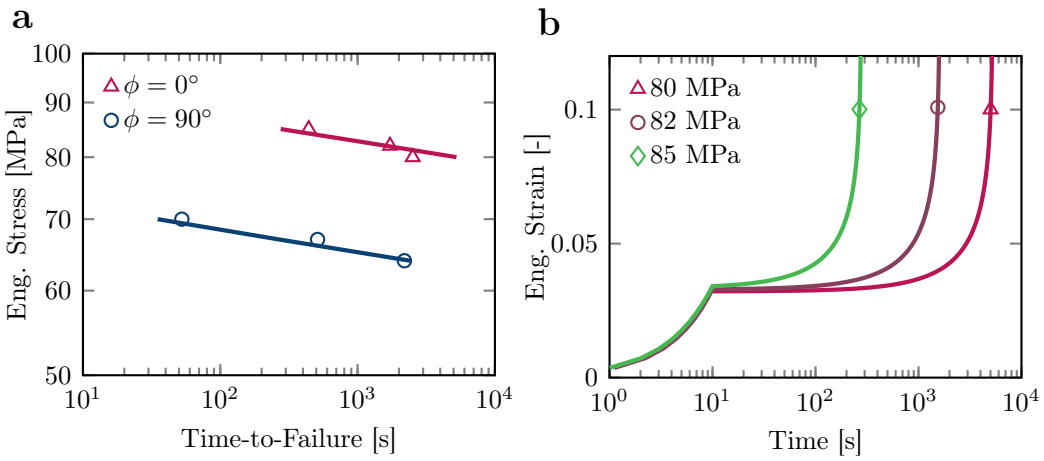

Figure 7: (a) Model predictions (solid-lines) vs. experimental data (markers) for time-to-failure at different stress levels; (b) engineering strain vs. time in the creep simulation for $\phi = 0°$ at different stress levels (markers show failure points).

ization at small strains. The focus has been on the proper prediction of the dependence of the yield stress on the orientation and strain rate. Evaluating the model's ability to predict the hardening for a more ductile material can be subject of a future research.

As Figure 8 shows, the model captures elastic anisotropy, however comparison with experimental data shows that the model can not predict the nonlinear pre-yield response accurately. As an example, the experimental data for the uniaxial test at $\phi = 0°$ is demonstrated by the markers in Figure 8. To improve the model prediction in the pre-yield regime, the model is extended to a multi-mode constitutive relation, in which, instead of a single relaxation time, a spectrum of relaxation times will be used. The multi-mode model will be discussed in the next section. It also should be noted that in the current single-mode model, as it is seen in Figure 8, elastic parameters are fitted in a way that with the linear approximation of the elastic regime,

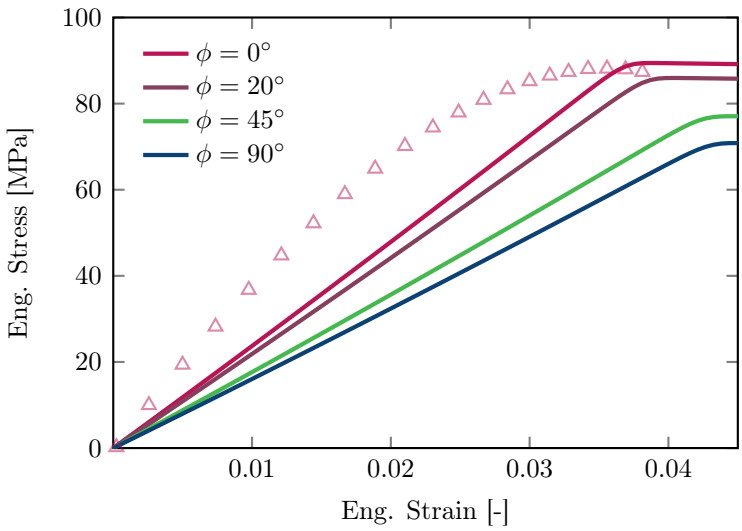

Figure 8: Model prediction for stress-strain curves for different material orientations at a strain rate of $\dot{\varepsilon} = 10^{-4}$ s^{-1}. Markers show the experimental results for $\phi = 0°$.

the strain at yield is captured with good accuracy.

5 Multi-Mode Model

Although the single-mode model predicts the yield stress with a good accuracy, it fails to capture the nonlinear pre-yield regime. This can be solved by using multiple relaxation times [22] where each relaxation time is represented by a distinct mode in the model. The model representation with multiple Maxwell branches is shown in Figure 9. In this case, the total stress is the summation of the stresses in different branches and Equation (7) can be rewritten as:

$$\boldsymbol{\sigma} = \boldsymbol{\sigma}_r + \sum_{i=1}^{n} \boldsymbol{\sigma}_{s,i}, \tag{32}$$

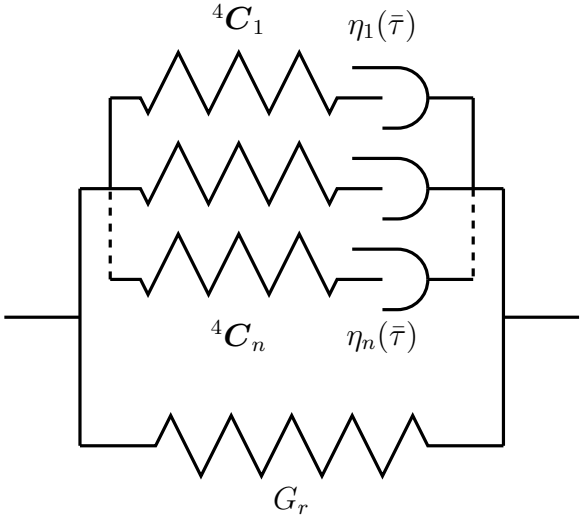

Figure 9: Mechanical analog of the multi-mode model.

where n is the number of modes. For thermorheologically simple materials, the stress shift factor (Equation (20)) is the same for all the modes and the viscosity for each mode is calculated according to:

$$\eta_i = \eta_{0,i}\, a(\bar{\tau}), \tag{33}$$

where $\bar{\tau}$ is the total equivalent stress, and the plastic flow at each branch is found as:

$$\dot{\bar{\gamma}}_{p,i} = \frac{\bar{\tau}_i}{\eta_i}, \tag{34}$$

$$\hat{\boldsymbol{D}}_{p,i} = \dot{\bar{\gamma}}_{p,i}\hat{\boldsymbol{N}}_i. \tag{35}$$

For finding the relaxation times and moduli of each mode, a characterization technique proposed by Van Breemen *et al.* [35] is used. This method,

which uses stress-time superposition [36], is developed for isotropic materials and it only requires a single stress-strain curve for finding properties of all the modes. In this paper, this method will be extended for the orthotropic response. In the isotropic method, first a discrete spectrum of relaxation times is chosen and then the moduli E_i of each mode are found through fitting the experimental data with the following Boltzmann integral [35]:

$$\hat{S}_s(t) = \sum_{i=1}^{n} \left[E_i \dot{\varepsilon} \int_{-\infty}^{t} \exp\left(-\frac{\psi - \psi'}{\lambda_i^{norm.}} \right) dt' \right], \tag{36}$$

where $\dot{\varepsilon}$ is the strain rate of the uniaxial test and $\hat{S}_s$ is the 2nd Piola-Kirchhoff stress in the uniaxial test. It should be noted that the superscript *norm* in λ_i^{norm} shows that this variable is the normal relaxation time for each mode, which can be related to the other model parameters using the following relation:

$$\lambda_i^{norm.} = \frac{\sigma_0}{E_i \dot{\varepsilon}_{0,i}} = \frac{3\tau_0}{E_i \dot{\gamma}_{0,i}}. \tag{37}$$

The variable ψ is called the stress-reduced time and ψ' is the pending stress reduced time [35]:

$$\begin{aligned} \psi &= \int_{-\infty}^{t} \frac{dt'}{a(\bar{\tau}(t'))}, \\ \psi' &= \int_{-\infty}^{t'} \frac{dt''}{a(\bar{\tau}(t''))}. \end{aligned} \tag{38}$$

The maximum and minimum relaxation times are chosen using the following relations and then the range is divided uniformly on a logarithmic scale. The number of modes is chosen such that there is an appropriate bal-

ance between accuracy and the computational cost. Usually, this number is chosen such that there exists one mode per decade. Choosing fewer relaxation times can lead to undesirable oscillations in the stress-strain response and more relaxation times increases the computational cost [35]:

$$\begin{aligned} \log(\lambda_{min}^{norm.}) &= \log(\psi(t=0)) - 1, \\ \log(\lambda_{max}^{norm.}) &= \log(\max(\psi)) + 1. \end{aligned} \tag{39}$$

This method has been successfully used for characterization of isotropic polymers. In this paper, this method will be extended for simple and efficient characterization of orthotropic materials by still using a single stress-strain curve. First, the same procedure as described above is used to find the moduli for a reference direction. Then it is assumed that the different orthotropic elastic parameters (i.e. E_{11}, E_{22}, G_{12},...) are distributed in the same way between different modes as the moduli in the reference direction. An exception is made for the Poisson ratios, which are assumed to be the same for all the branches. For example, for the reference direction $\phi = 90°$, the distribution of the moduli is described by the dimensionless parameters m_i as:

$$\begin{aligned} E_{22} &= \sum_{i=1}^{n} E_{22,i} = \sum_{i=1}^{n} m_i E_{22}, \\ \sum_{i=1}^{n} m_i &= 1, \end{aligned} \tag{40}$$

where E_{22} is the total modulus in the $\phi = 90°$ direction and $E_{22,i}$ is the modulus in this direction for mode i. Using the assumption of the same distribution of orthotropic elastic properties, the following can be written:

Table 2: Elastic parameters for the multi-mode model.

E_{11} [MPa]	E_{22} [MPa]	G_{12} [MPa]	$\nu_{12} = \nu_{23}$
4181	2988	1184	0.26

$$ {}^4\boldsymbol{C}_i = m_i \, {}^4\boldsymbol{C}, \tag{41} $$

where ${}^4\boldsymbol{C}_i$ is the elastic stiffness tensor of mode i and ${}^4\boldsymbol{C}$ is the total elastic stiffness tensor. Using this formulation, the characterization method is easily extended to the orthotropic case.

Relaxation times and moduli for different modes are found using the stress-strain curve at $\phi = 90^\circ$ for the rate of 10^{-4} s^{-1}. The obtained parameters are shown in Table 3. As it is shown in this table, the maximum relaxation time is of the order of 10^{22} s and 23 modes are used, corresponding to one mode per decade. The characteristic stress τ_0, is the same as the value shown in Table 1, and is found from the change of the yield stress with the strain rate at $\phi = 90^\circ$ (Figure 4). Figure 10 shows the obtained characteristic relaxation modulus in the reference direction. Using Equation (41), the elastic stiffness tensor for each mode is found. Values for the total elastic parameters which are found using the initial slopes of the experimental stress-strain curves (Figure 2 (b)) are shown in Table 2.

The multi-mode model has been implemented in ABAQUS UMAT. The same implicit scheme as presented for the single-mode method is used for numerical integration. The extension of the numerical procedure to the multi-mode method is straightforward. Stress is updated in each branch and then the total stress is found by summation of all stress values.

The simulation results for a uniaxial test under constant strain rate for different material orientations are compared with the experiments in Figure 11. As it is seen in Figure 11, now the nonlinear pre-yield regime is captured with a good accuracy for different orientations. Although only the stress-strain curve in $\phi = 90^\circ$ direction was used to find the moduli and relaxation times for different modes, the predictions for other directions match the experiments very well. As was shown in Figure 8, although the single-mode, captures the yield behavior accurately, it is unable to provide a good estimation of the elastic response. However, the multi-mode model requires more computational time, because of the bigger number of the branches. Whenever the solution time can be favored over the improved accuracy in the elastic regime, the single-mode method can be chosen, otherwise, the multi-mode method provides very good accuracy both for the elastic and the yield behavior. The multi-mode model is also able to predict the effect of the strain rate on the elastic response. As an example, Figure 12, shows the model prediction vs. experimental data when the strain rate changes to 10^{-6} s^{-1}. As it is shown in this graph, the viscoelastic response is also modeled with a good accuracy.

6 Conclusion

In this study, an anisotropic viscoelastic-viscoplastic macro-mechanical model was presented for short-fiber reinforced polymers. The model captures the effects of both material orientation and loading rate on the yield behavior.

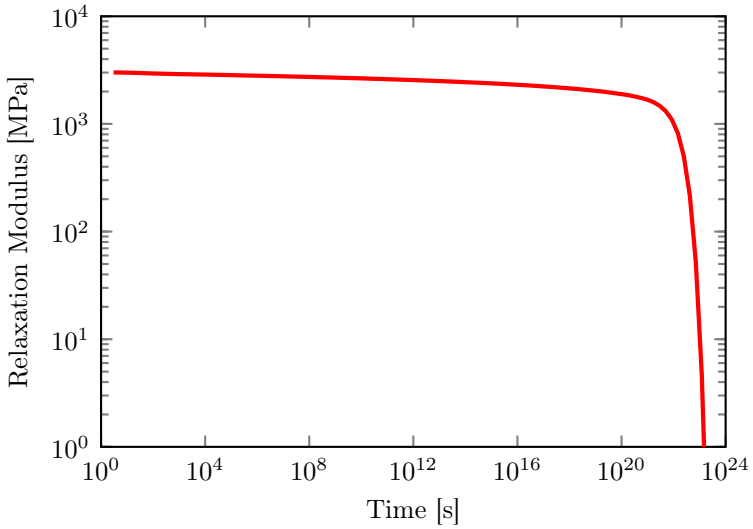

Figure 10: Relaxation modulus versus time for $\phi = 90°$.

Table 3: Normal relaxation times, moduli and zero shear viscosities for different modes, fitted using using a uniaxial test for $\phi = 90°$ and $\dot{\varepsilon} = 10^{-4}$ s^{-1}.

Mode	$\lambda_i^{norm.}$[s]	$E_{22,i}$[MPa]	$\eta_{0,i}$[MPa s]
1	2.07×10^{22}	1659	1.14×10^{25}
2	1.81×10^{21}	164	9.91×10^{22}
3	2.07×10^{20}	136	9.39×10^{21}
4	2.37×10^{19}	118	9.36×10^{20}
5	2.71×10^{18}	93	8.40×10^{19}
6	3.10×10^{17}	83	8.61×10^{18}
7	3.54×10^{16}	71	8.43×10^{17}
8	4.05×10^{15}	65	8.76×10^{16}
9	4.63×10^{14}	56	8.65×10^{15}
10	5.29×10^{13}	57	9.99×10^{14}
11	6.04×10^{12}	49	9.81×10^{13}
12	6.91×10^{11}	47	1.09×10^{13}
13	7.90×10^{10}	42	1.10×10^{12}
14	9.03×10^{9}	43	1.30×10^{11}
15	1.03×10^{9}	37	1.27×10^{10}
16	1.18×10^{8}	36	1.41×10^{9}
17	1.35×10^{7}	36	1.62×10^{8}
18	1.54×10^{6}	27	1.40×10^{7}
19	1.76×10^{5}	39	2.31×10^{6}
20	2.01×10^{4}	28	1.86×10^{5}
21	2.30×10^{3}	25	1.89×10^{4}
22	2.63×10^{2}	44	3.84×10^{3}
23	3.01×10^{1}	59	5.91×10^{2}

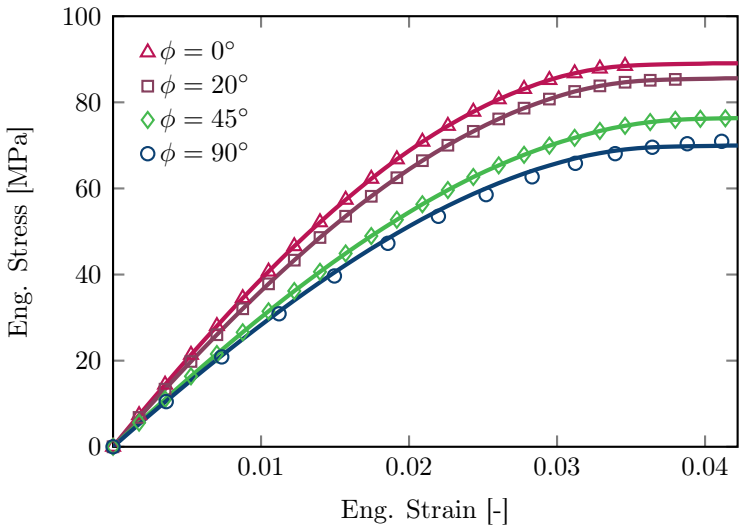

Figure 11: Multi-mode model predictions (solid lines) vs. experimental data (markers) for different material orientations at a strain rate of 10^{-4} s^{-1}.

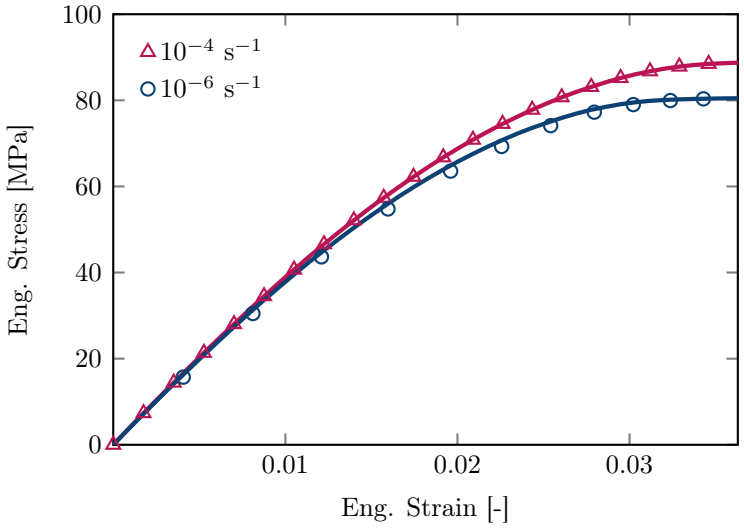

Figure 12: Multi-mode model predictions (solid lines) vs. experimental data (markers) for different strain rates at $\phi = 0°$.

The uniaxial tests performed at different strain rates and material orientations showed these effects are decoupled. The presented model is constructed such that, this effect is captured. An implicit integration scheme was used for the numerical implementation of the model as a UMAT in ABAQUS. The experimental results were used for validation of the model and a good agreement was observed in the prediction of the yield behavior. The model accuracy in the pre-yield regime was successfully improved by extending the model to a multi-mode version. An efficient method for finding the parameters of the multi-mode model was proposed.

Acknowledgement

This research forms part of the research programme of DPI, project #786ft15.

References

[1] M. De Monte, E. Moosbrugger, and M. Quaresimin. Influence of temperature and thickness on the off-axis behaviour of short glass fibre reinforced polyamide 6.6 – quasi-static loading. *Composites Part A: Applied Science and Manufacturing*, 41(7):859–871, 2010.

[2] K. Tanaka, T. Kitano, and N. Egami. Effect of fiber orientation on fatigue crack propagation in short-fiber reinforced plastics. *Engineering Fracture Mechanics*, 123:44–58, 2014.

[3] M.F. Arif, N. Saintier, F. Meraghni, J. Fitoussi, Y. Chemisky, and G. Robert. Multiscale fatigue damage characterization in short glass

fiber reinforced polyamide-66. *Composites Part B: Engineering*, 61:55–65, 2014.

[4] J.D. Eshelby. The determination of the elastic field of an ellipsoidal inclusion, and related problems. *Proceedings of the Royal Society of London. Series A. Mathematical and Physical Sciences*, 241(1226):376–396, 1957.

[5] Z. Hashin and S. Shtrikman. A variational approach to the theory of the elastic behaviour of multiphase materials. *Journal of the Mechanics and Physics of Solids*, 11(2):127–140, 1963.

[6] K. Tanaka and T. Mori. The hardening of crystals by non-deforming particles and fibres. *Acta Metallurgica*, 18(8):931–941, 1970.

[7] G.P. Tandon and G.J. Weng. The effect of aspect ratio of inclusions on the elastic properties of unidirectionally aligned composites. *Polymer Composites*, 5(4):327–333, 1984.

[8] Y. Benveniste. A new approach to the application of mori-tanaka's theory in composite materials. *Mechanics of Materials*, 6(2):147–157, 1987.

[9] H.J. Böhm, A. Eckschlager, and W. Han. Multi-inclusion unit cell models for metal matrix composites with randomly oriented discontinuous reinforcements. *Computational Materials Science*, 25(1):42–53, 2002.

[10] H.R. Lusti, P.J. Hine, and A.A. Gusev. Direct numerical predictions for the elastic and thermoelastic properties of short fibre composites. *Composites Science and Technology*, 62(15):1927–1934, 2002.

[11] S. Kari, H. Berger, and U. Gabbert. Numerical evaluation of effective material properties of randomly distributed short cylindrical fibre composites. *Computational Materials Science*, 39(1):198–204, 2007. Proceedings of the 15th International Workshop on Computational Mechanics of Materials.

[12] A. Dean, S. Sahraee, J. Reinoso, and R. Rolfes. Finite deformation model for short fiber reinforced composites: Application to hybrid metal-composite clinching joints. *Composite Structures*, 151:162–171, 2016. Smart composites and composite structures In honour of the 70th anniversary of Professor Carlos Alberto Mota Soares.

[13] D. Notta-Cuvier, F. Lauro, B. Bennani, and R. Balieu. Damage of short-fibre reinforced materials with anisotropy induced by complex fibres orientations. *Mechanics of Materials*, 68:193–206, 2014.

[14] R.N. Haward and G. Thackray. The use of a mathematical model to describe isothermal stress-strain curves in glassy thermoplastics. In *Proc. R. Soc. Lond. A*, volume 302, pages 453–472. The Royal Society, 1968.

[15] M.C. Boyce, D.M. Parks, and A.S. Argon. Large inelastic deformation of glassy polymers. part i: rate dependent constitutive model. *Mechanics of Materials*, 7(1):15–33, 1988.

[16] E.M. Arruda and M.C. Boyce. Evolution of plastic anisotropy in amorphous polymers during finite straining. *International Journal of Plasticity*, 9(6):697–720, 1993.

[17] O.A. Hasan, M.C. Boyce, X.S. Li, and S. Berko. An investigation of the yield and postyield behavior and corresponding structure of poly (methyl methacrylate). *Journal of polymer science part B: polymer physics*, 31(2):185–197, 1993.

[18] C.P. Buckley and D.C. Jones. Glass-rubber constitutive model for amorphous polymers near the glass transition. *Polymer*, 36(17):3301–3312, 1995.

[19] C.P. Buckley, P.J. Dooling, J. Harding, and C. Ruiz. Deformation of thermosetting resins at impact rates of strain. part 2: constitutive model with rejuvenation. *Journal of the Mechanics and Physics of Solids*, 52(10):2355–2377, 2004.

[20] J.J. Wu and C.P. Buckley. Plastic deformation of glassy polystyrene: a unified model of yield and the role of chain length. *Journal of Polymer Science Part B: Polymer Physics*, 42(11):2027–2040, 2004.

[21] L.E. Govaert, P.H.M. Timmermans, and W.A.M. Brekelmans. The influence of intrinsic strain softening on strain localization in polycarbonate: modeling and experimental validation. *Journal of Engineering Materials and Technology*, 122(2):177–185, 2000.

[22] T.A. Tervoort, E.T.J. Klompen, and L.E. Govaert. A multi-mode approach to finite, three-dimensional, nonlinear viscoelastic behavior of polymer glasses. *Journal of Rheology*, 40(5):779–797, 1996.

[23] E.T.J. Klompen, T.A.P. Engels, L.E. Govaert, and H.E.H. Meijer. Modeling of the postyield response of glassy polymers: influence of thermomechanical history. *Macromolecules*, 38(16):6997–7008, 2005.

[24] T.B. van Erp, C.T. Reynolds, T. Peijs, J.A.W. van Dommelen, and L.E. Govaert. Prediction of yield and long-term failure of oriented polypropylene: Kinetics and anisotropy. *Journal of Polymer Science Part B: Polymer Physics*, 47(20):2026–2035, 2009.

[25] D.J.A. Senden, G.W.M. Peters, L.E. Govaert, and J.A.W. Van Dommelen. Anisotropic yielding of injection molded polyethylene: Experiments and modeling. *Polymer*, 54(21):5899–5908, 2013.

[26] H. Eyring. Viscosity, plasticity, and diffusion as examples of absolute reaction rates. *The Journal of chemical physics*, 4(4):283–291, 1936.

[27] J.N. Reddy. *Mechanics of laminated composite plates and shells: theory and analysis*. Boca Raton: CRC press, 2003.

[28] T.A. Tervoort, R.J.M. Smit, W.A.M. Brekelmans, and L.E. Govaert. A constitutive equation for the elasto-viscoplastic deformation of glassy polymers. *Mechanics of Time-Dependent Materials*, 1(3):269–291, 1997.

[29] R. Hill. A theory of the yielding and plastic flow of anisotropic metals. *Proc. R. Soc. Lond. A*, 193(1033):281–297, 1948.

[30] E.J. Kramer and E.W. Hart. Theory of slow, steady state crack growth in polymer glasses. *Polymer*, 25(11):1667–1678, 1984.

[31] M.F. Kanninen and C.H. Popelar. *Advanced fracture mechanics*. Number 15. Oxford University Press, 1985.

[32] J.M. Crissman and G.B. McKenna. Relating creep and creep rupture in pmma using a reduced variable approach. *Journal of Polymer Science Part B: Polymer Physics*, 25(8):1667–1677, 1987.

[33] M.J. Mindel and N. Brown. Creep and recovery of polycarbonate. *Journal of Materials Science*, 8(6):863–870, 1973.

[34] C. Bauwens-Crowet, J.M. Ots, and J.C. Bauwens. The strain-rate and temperature dependence of yield of polycarbonate in tension, tensile creep and impact tests. *Journal of Materials Science*, 9(7):1197–1201, 1974.

[35] L.C.A. van Breemen, E.T.J. Klompen, L.E. Govaert, and H.E.H. Meijer. Extending the egp constitutive model for polymer glasses to multiple relaxation times. *Journal of the Mechanics and Physics of Solids*, 59(10):2191–2207, 2011.

[36] H. Leaderman. *Elastic and creep properties of filamentous materials and other high polymers*. Washington, D.C: The Textile Foundation, 1943.

Appendix

Consistent Tangent Stiffness Matrix

Derivation of the tangent stiffness matrix consistent with the presented implicit integration scheme is presented in this section. The index notation is used in the derivation of the stiffness tensor. The comma in the subscripts is used for separating the indices from the other subscripts and it does not represent a derivative with respect to the coordinates. For simplicity, the subscript $n+1$ is eliminated and unless otherwise is stated, the variables are associated with time t_{n+1}. The starting point for the calculation of the consistent tangent stiffness tensor $\partial\boldsymbol{\sigma}/\partial\boldsymbol{F}$, is taking the derivative of the plastic right stretch tensor $\boldsymbol{U}_p$ with respect to the deformation gradient tensor $\boldsymbol{F}$:

$$U_{p,ij} = F^{-1}_{e,ik} F_{kj}, \tag{A.1}$$

$$\frac{\partial U_{p,ij}}{\partial F_{mn}} = \frac{\partial F^{-1}_{e,ik}}{\partial F_{e,rs}} \frac{\partial F_{e,rs}}{\partial F_{mn}} F_{kj} + F^{-1}_{e,ik} \frac{\partial F_{kj}}{\partial F_{mn}}. \tag{A.2}$$

The derivative of the plastic right Cauchy-Green deformation tensor is calculated according to:

$$C_{p,ij} = U_{p,iw} U_{p,wj}, \tag{A.3}$$

$$\frac{\partial C_{p,ij}}{\partial F_{mn}} = \frac{\partial U_{p,iw}}{\partial F_{mn}} U_{p,wj} + U_{p,iw} \frac{\partial U_{p,wj}}{\partial F_{mn}}. \tag{A.4}$$

The derivative of the plastic rate of deformation tensor $\boldsymbol{D}_p$, is obtained by:

$$\hat{D}_{p,ij} = \dot{\bar{\gamma}}_p \hat{N}_{ij}, \tag{A.5}$$

$$\frac{\partial \hat{D}_{p,ij}}{\partial F_{mn}} = \frac{\partial \dot{\bar{\gamma}}_p}{\partial F_{mn}} \hat{N}_{ij} + \dot{\bar{\gamma}}_p \frac{\partial \hat{N}_{ij}}{\partial \hat{S}_{s,kl}} \frac{\partial \hat{S}_{s,kl}}{\partial F_{e,rs}} \frac{\partial F_{e,rs}}{\partial F_{mn}}. \tag{A.6}$$

The derivative of the rate of the equivalent plastic strain $\dot{\bar{\gamma}}_p$ with respect to the deformation gradient $\boldsymbol{F}$ can be found as follows:

$$\dot{\bar{\gamma}}_p = \frac{\bar{\tau}}{\eta}, \tag{A.7}$$

$$\frac{\partial \dot{\bar{\gamma}}_p}{\partial F_{mn}} = \frac{1}{\eta} \hat{N}_{kl} \frac{\partial \hat{S}_{s,kl}}{\partial F_{e,rs}} \frac{\partial F_{e,rs}}{\partial F_{mn}}. \tag{A.8}$$

Knowing the derivative of the plastic rate of deformation $\hat{\boldsymbol{D}}_p$, the derivative of the rate of the plastic right Cauchy-Green deformation tensor can be found:

$$\dot{C}_{p,ij} = 2 U_{p,ri} \hat{D}_{p,rs} U_{p,sj}, \tag{A.9}$$

$$\frac{\partial \dot{C}_{p,ij}}{\partial F_{mn}} = 2 \frac{\partial U_{p,ri}}{\partial F_{mn}} \hat{D}_{p,rs} U_{p,sj} + 2 U_{p,ri} \frac{\partial \hat{D}_{p,rs}}{\partial F_{mn}} U_{p,sj} + 2 U_{p,ri} \hat{D}_{p,rs} \frac{\partial U_{p,sj}}{\partial F_{mn}}. \tag{A.10}$$

The plastic right Cauchy-Green deformation tensor $\boldsymbol{C}_p$ can be found from the following backward integration:

$$C_{p,ij} = C_{p_n,ij} + \Delta t \dot{C}_{p,ij}, \tag{A.11}$$

where $\boldsymbol{C}_{p_n}$ is the plastic right Cauchy-Green deformation tensor at time t_n. Taking the derivative of both sides with respect to the deformation gradient $\boldsymbol{F}$ gives:

$$\frac{\partial C_{p,ij}}{\partial F_{mn}} = \Delta t \frac{\partial \dot{C}_{p,ij}}{\partial F_{mn}}. \tag{A.12}$$

The left and right hand sides of this equation can be substituted using Equation (A.4) and Equation (A.10) respectively:

$$\begin{aligned}\frac{1}{\Delta t}\left(\frac{\partial U_{p,iw}}{\partial F_{mn}} U_{p,wj} + U_{p,iw}\frac{\partial U_{p,wj}}{\partial F_{mn}}\right) =& 2\frac{\partial U_{p,ri}}{\partial F_{mn}}\hat{D}_{p,rs}U_{p,sj} + \\ & 2U_{p,ri}\frac{\partial \hat{D}_{p,rs}}{\partial F_{mn}}U_{p,sj} + 2U_{p,ri}\hat{D}_{p,rs}\frac{\partial U_{p,sj}}{\partial F_{mn}}.\end{aligned} \tag{A.13}$$

Substituting $\partial \boldsymbol{U}_p/\partial \boldsymbol{F}$ from Equation (A.2), $\partial \hat{\boldsymbol{D}}_p/\partial \boldsymbol{F}$ from Equations (A.6) and (A.8), a set of linear equations for $\partial \boldsymbol{F}_e/\partial \boldsymbol{F}$, is obtained. By solving this set of equations, the stiffness tensor is found. The first part of the stiffness tensor is associated with the driving stress $\boldsymbol{\sigma}_s$ and can be calculated according to:

$$K_{s,ijmn} = \frac{\partial \sigma_{s,ij}}{\partial F_{mn}} = \frac{\partial \sigma_{s,ij}}{\partial F_{e,pq}}\frac{\partial F_{e,pq}}{\partial F_{mn}}, \tag{A.14}$$

where $\partial \boldsymbol{\sigma}_s/\partial \boldsymbol{F}_e$ can be easily found from the anisotropic elastic relation. The next part of the stiffness tensor is calculated by finding the derivative of the hardening stress $\boldsymbol{\sigma}_r$:

$$K_{r,ijmn} = \frac{\partial \sigma_{r,ij}}{\partial F_{mn}}. \tag{A.15}$$

Finally, the total stiffness tensor is found by summation of the different contributions:

$$\frac{\partial \sigma_{ij}}{\partial F_{mn}} = K_{s,ijmn} + K_{r,ijmn}. \tag{A.16}$$